Supporting Information

Modulation of lithium ion transport kinetics in polymer-based electrolytes by defect engineering for ultralong-cycle solid-state lithium metal batteries

Yunpeng Qu[a], Lin Wang[a], Changxing Han[a], Borui Li[a], Wenkai Song[a], Chang Su[a], Wanyuan Jiang[b], Dongming Liu[a], Mengfan Pei[a], Xin Jin[a], Shuo Zhuo[a], Runyang Li[a], Jinfeng Zhang[a], Xigao Jian[a,b,], and Fangyuan Hu[a,]**

[a] Dr. Y. Qu, Dr. L. Wang, Dr. C. Han, Dr. B. Li, Dr. W. Song, Dr. C. Su, Dr. D. Liu, Dr. M. Pei, Dr. X. Jin, Dr. S. Zhuo, R. Li, J. Zhang, Prof. X. Jian, Prof. F. Hu
School of Materials Science and Engineering, State Key Laboratory of Fine Chemicals, Frontiers Science Center for Smart Materials Oriented Chemical Engineering, Technology Innovation Center of High Performance Resin Materials (Liaoning Province), Dalian University of Technology, Dalian 116024, China.
E-mail: hufangyuan@dlut.edu.cn (Fangyuan Hu)

[b] Dr. W. Jiang, Prof. X. Jian
State Key Laboratory of Fine Chemicals, Frontiers Science Center for Smart Materials Oriented Chemical Engineering, School of Chemical Engineering, Technology Innovation Center of High Performance Resin Materials (Liaoning Province), Dalian University of Technology, Dalian 116024, China.
E-mail: jian4616@dlut.edu.cn (Xigao Jian)

Experimental section

1. Materials preparation

Molybdenum sulfide (MoS_2, >99.5%) and succinonitrile (SN, 99%) were purchased from Macklin without further purification. Copper nanopowder (>99.9%) was purchased from Aladdin without further purification. Poly(vinylidene fluoride-co-hexafluoropropylene) (PVDF-HFP) was purchased from Sigma-Aldrich without further purification. Lithium bis(trifluoromethanesulfonyl)imide (LiTFSI) and N,N-Dimethylformamide (DMF) were purchased from DoDoChem. Super P, polyvinylidene difluoride (PVDF), lithium iron(II) phosphate (LFP) and lithium nickel manganese cobalt oxide (NCM811) were purchased from Canrd.

2. Preparation of LFP and NCM811 cathode

LFP, Super P, LiTFSI and PVDF were stirred at a mass ratio of 7.5:1:0.5:1 until the formation of the viscous slurry. The slurry was coated on the carbon-coated aluminum foil and dried at 60°C under vacuum to obtain the cathode. The loading mass of the LFP cathode active material is 1.6-2 mg.

NCM811, Super P, LiTFSI, SN and PVDF were stirred at a mass ratio of 7.5:0.8:0.5:0.4:0.8 until the formation of the viscous slurry. The slurry was coated on the carbon-coated aluminum foil and dried at 60°C under vacuum to obtain the cathode. The loading mass of the NCM811 cathode active material exceeds 2.2 mg.

3. Coin cell assembly

The stainless steel (SS) symmetric cells, Li||SS cells, Li||Li symmetric cells, Li||Cu cells, LFP||Li full cells and NCM811||Li full cells were all assembled in the following way: cathode, polymer electrolyte, anode, stainless steel gasket, stainless steel shrapnel. All of the cells were assembled using CR2032 coin cells. The above steps are performed in a glove box in an Ar gas atmosphere (O_2 and H_2O below 0.5 ppm).

4. Pouch cell assembly

For LFP||Li pouch cells, LFP (80% wt%), Super P (10 wt%), LiTFSI (5 wt%) and PVDF binder (5 wt%) were mixed well with appropriate amounts of NMP to form a viscous slurry. The obtained slurry was coated on the carbon-coated Al foil, which was

then dried at 60°C for 24 h, resulting in a LFP cathode for use in the pouch-cell assembly. The loading mass of the LFP cathode active material is 17.4 mg cm^{-2}. The LFP cathode dimensions are 56 mm × 43 mm. Li foils were used as the anodes. The Al-plastic film was used as the packaging material.

5. Materials characterizations

Fourier transform infrared spectroscopy (FTIR) were performed on Thermo-Fisher 6700. The chemical composition of the obtained products was characterized by X-ray photoelectron spectroscope (XPS, ESCALAB 250). The morphology of the samples was characterized by scanning electron microscopy (SEM, Hitachi, SU8220). The microstructural characterisation of the material was carried out by spherical aberration-corrected transmission electron microscopy (AC-TEM, JEM-ARM300F2) and transmission electron microscope (TEM, Tecnai G2 F30 S-Twin). Thermogravimetric analysis (TGA) was tested on a Mettler TGA/SDTA851 TGA thermal analyzer at a heating rate of 10°C min^{-1} in N_2 from 30°C to 800°C. The 3D reconstruction images of PHMS were observed by Hitachi Xradia 610 Versa microscope. Confocal micro-Raman spectra was tested on an Invia Qontor. The characterization of the sulphur vacancy (S-V) was confirmed by electron paramagnetic resonance spectroscopy (EPR, E500) analysis.

6. Electrochemical tests

Electrochemical impedance spectroscopy (EIS) was used to measure the ionic conductivity of the electrolytes between 10 mHz to 100 kHz with an AC amplitude of 10 mV of the SS||SS symmetric cells. The ionic conductivity was calculated from equation:

$$\sigma = \frac{L}{SR}$$

where L is the distance between stainless steel; S is the area of the stainless steel; and R is the impedance.

The electrochemical stability of the electrolytes was evaluated by linear sweep voltammetry (LSV) experiment performed with carbon-coated aluminum foil as a working electrode, Li metal as a counter and reference electrode from 0 V to 5.5 V vs.

Li/Li^+ at a scanning rate of 0.1 mV s^{-1}.

The Li^+ transference number (t_{Li^+}) was measured and calculated by the following formula:

$$t_{Li^+} = \frac{I_s(\Delta V - I_0 R_0)}{I_0(\Delta V - I_s R_s)}$$

where I_0 and I_s are the initial and steady-state current, respectively, R_0 and R_s are the initial and steady-state ohmic resistance, respectively, and ΔV (10 mV) is the potential applied to the cell.

The CV tests (potential window -0.2-0.2 V) and EIS (10 mHz-100 kHz) were measured on a VMP-3 multichannel workstation.

The galvanostatic discharge/charge, rate and cycling performance measurements were conducted on the LAND CT2001A test system with different voltage ranges.

7. Theoretical calculations

The CASTEP (Cambridge Serial Total Energy Package) module of the Materials Studio software is utilised for all calculations. The PBE (Perdew-Burke-Ernzerhof) generalised function under the generalised gradient approximation (GGA) is selected as the correlation function for the exchange of electrons, and the self-conjugate field (SCF) method is employed to solve the Kohn-Sham equation. The convergence value of the self-consistent field energy is determined to be 1.0×10^{-6} eV/atom. The total energy error of the system is found to be within 1.0×10^{-7} eV/atom, the stress deviation is less than 0.02 GPa, and the convergence criterion of the atomic force is established as 0.01 eV/Å. The k-point sampling in the Brillouin zone is conducted utilising the Monkhorst-Pack grid. A total of $9 \times 9 \times 2$ k-points are selected for the calculation, employing the plane wave method. The truncation energy of the basis vectors is set to 440 eV, and the ultra-soft pseudopotential is employed to model the interaction between the ion nuclei and the valence electrons. In order to guarantee the precision of the calculation outcomes, it is imperative to optimise the structure of each cell in conjunction with the cell parameters and atomic coordinates. The construction of an interface model is predicated on the optimised surface model. This is then subjected to

further optimisation, thus resulting in the calculation of the relevant properties.

Supporting Figures

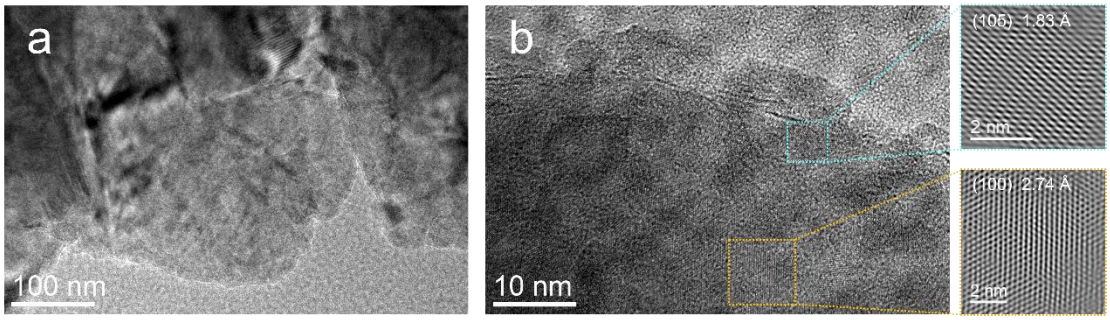

Figure S1. HRTEM images the prepared MoS_x.

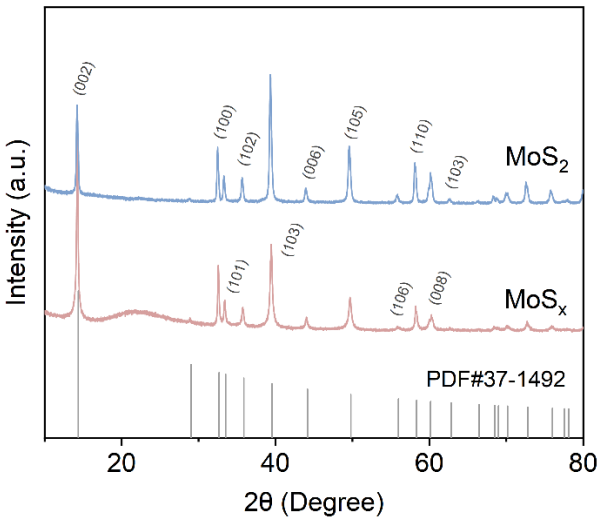

Figure S2. XRD patterns of MoS_2, MoS_x, and hexagonal MoS_2 (No. 37-1492).

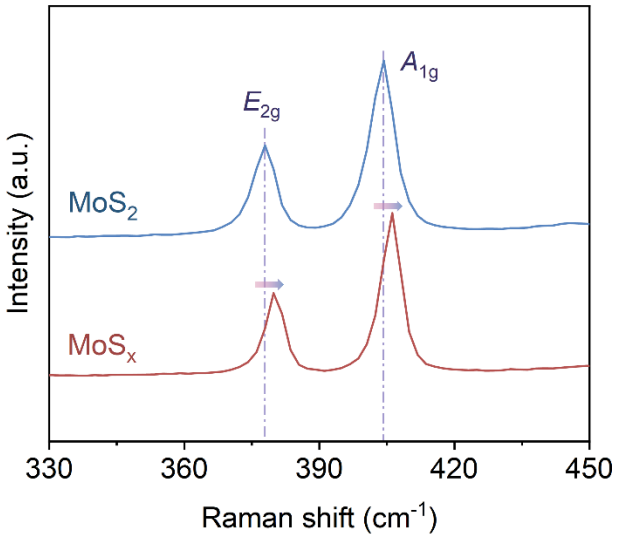

Figure S3. Raman spectra of MoS_x and MoS_2.

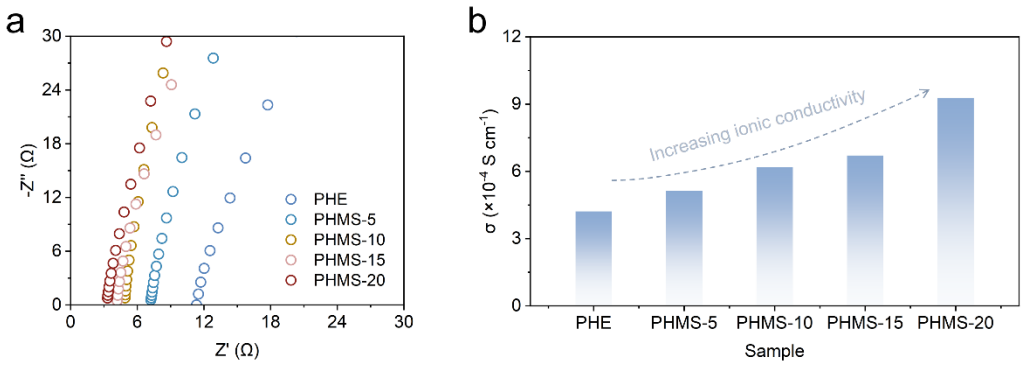

Figure S4. Test results for ionic conductivity of electrolytes at different MoS_x addition levels.

We incorporated the prepared MoS_x filler into the PVDF-HFP matrix at varying ratios, assembled stainless steel symmetric cells, and similarly tested their ionic conductivity at 30°C. As shown in **Figure S4**, with increasing addition levels, the overall vacancy concentration also rises, leading to an increase in ionic conductivity. The ionic conductivity reached its maximum values when the MoS_x filler content was increased to 15% and 20%. However, excessive addition of MoS_x filler prevents uniform dispersion of the nanoparticles within the prepared precursor solution, leading to agglomeration at a 20% loading. Consequently, we selected a nanofiller loading of 15% and proceeded with the subsequent series of tests according to the aforementioned experimental protocol.

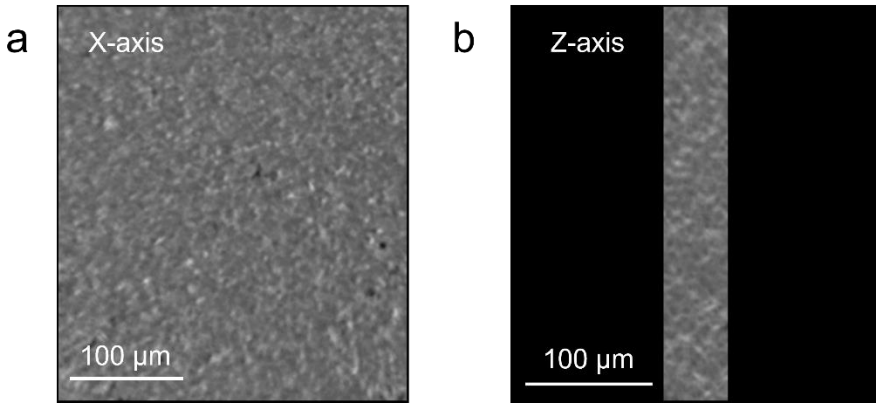

Figure S5. XRM-CT 2D section images of PHMS.

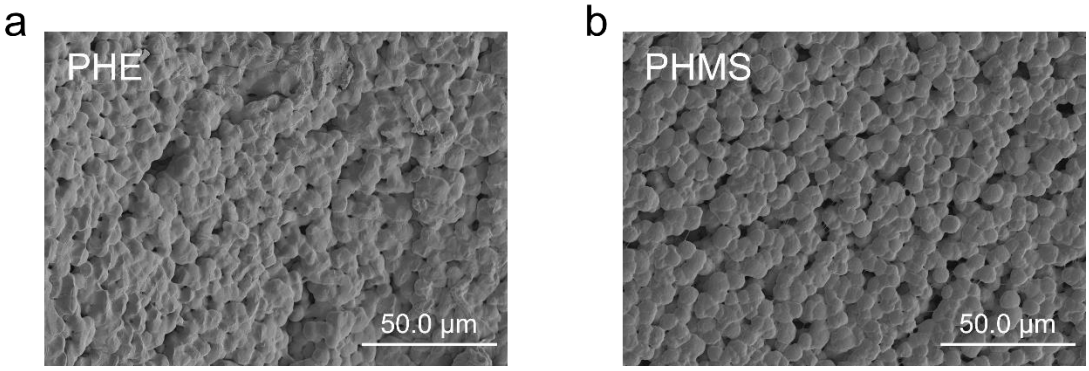

Figure S6. SEM images of PHE and PHMS.

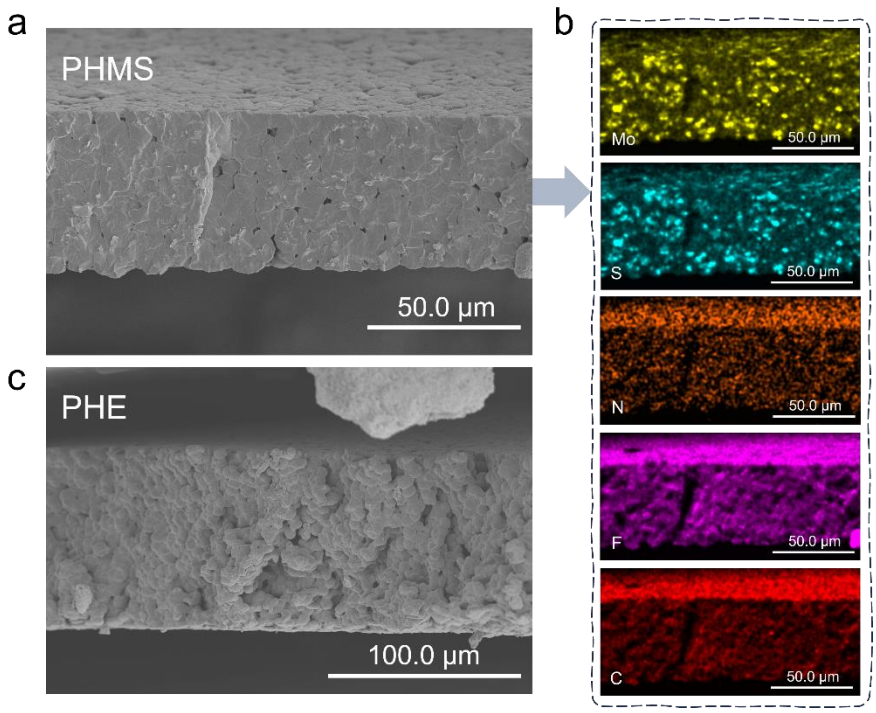

Figure S7. (a)-(b) Cross-sectional image of PHMS and corresponding EDS images. (c) Cross-sectional image of PHE.

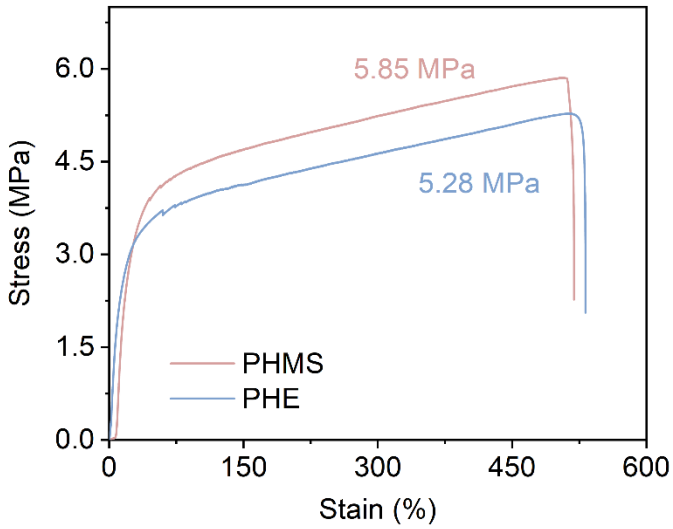

Figure S8. Tensile modulus of elasticity of PHE and PHMS electrolytes.

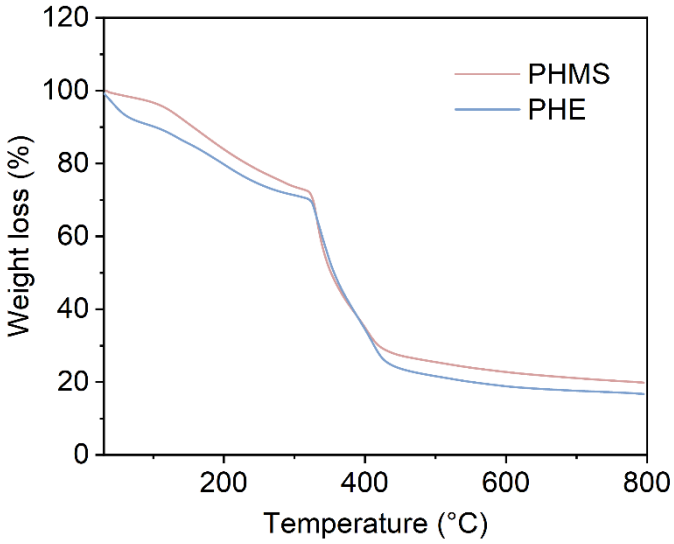

Figure S9. TGA tests of PHE and PHMS.

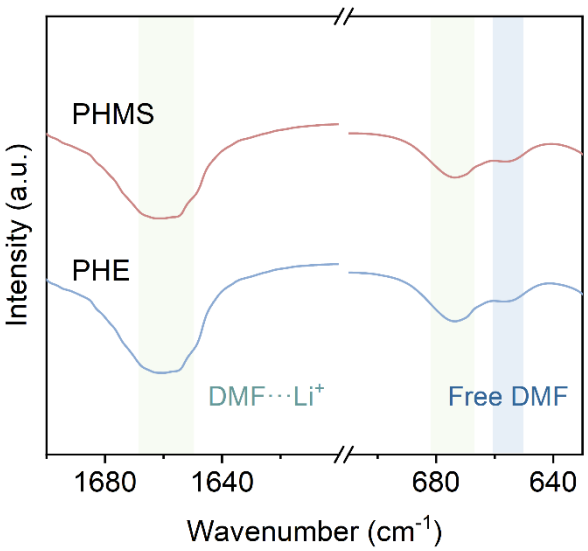

Figure S10. FT-IR spectral analysis of PHE and PHMS.

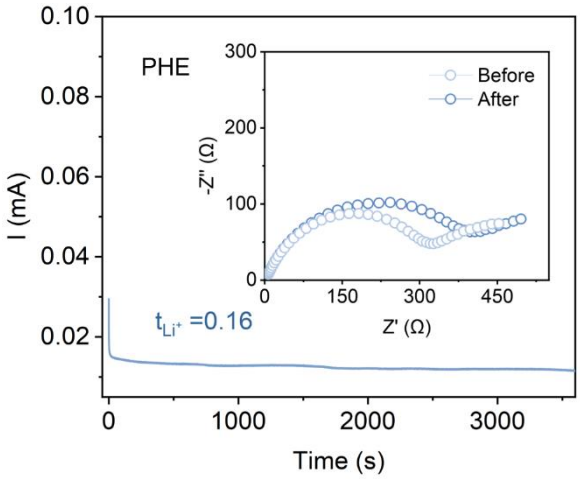

Figure S11. Li-ion transfer number test of PHE. The insets are the related Nyquist plots of cells before and after testing.

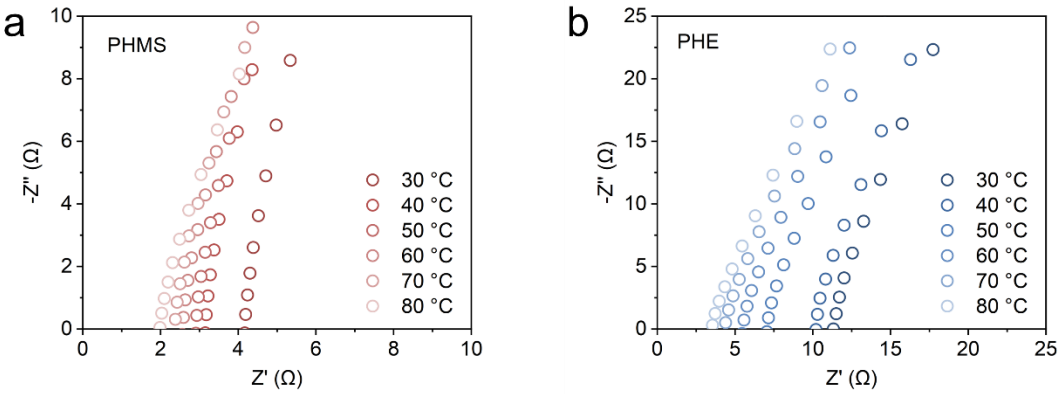

Figure S12. Nyquist impedance spectra of SS||SS batteries using PHE and PHMS.

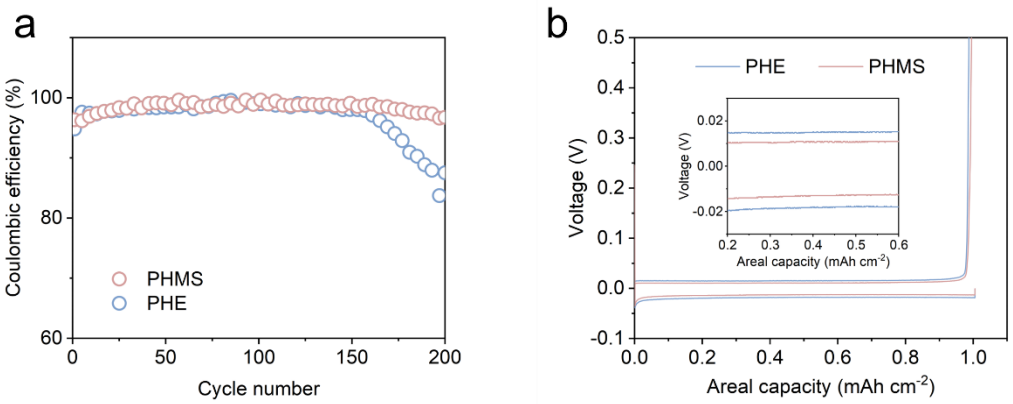

Figure S13. (a) Cycling tests of Li||Cu cells with different electrolytes.

(b) Polarization curves of Li||Cu cells with different electrolytes at the 50th cycle.

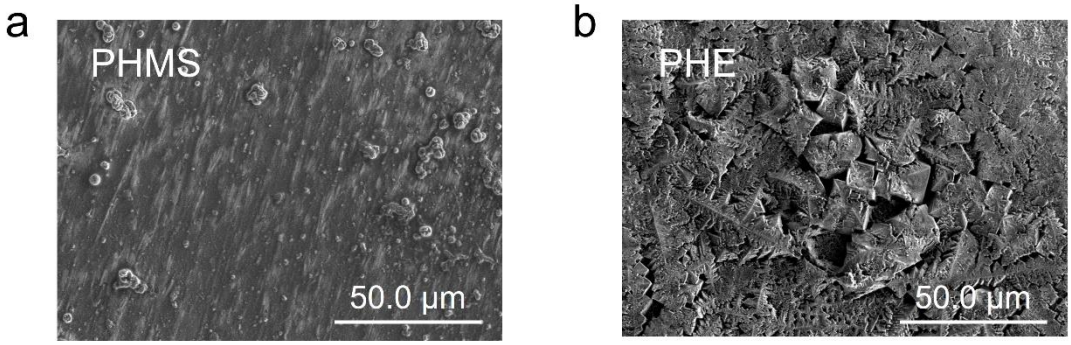

Figure S14. SEM images of lithium morphology deposited on the surface of copper foil after cycling (a) PHMS; (b) PHE.

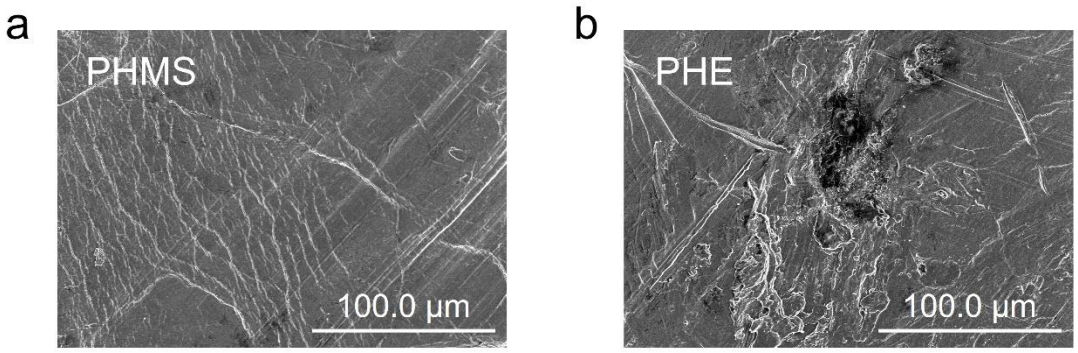

Figure S15. SEM images of the surface morphology of the lithium metal anode after cycling (a) PHMS; (b) PHE.

In the PHMS system containing defect-rich fillers, lithium deposition exhibits a uniform, dense morphology with a smooth surface devoid of discernible defects. This is primarily attributed to the defect-rich fillers optimizing interfacial ion transport and inducing the formation of a stable SEI film rich in inorganic components, possessing high ionic conductivity and mechanical strength. This interfacial phase effectively suppresses the nucleation and growth of lithium dendrites while reducing side reactions. In contrast, within the PHE system lacking fillers, we observed extensive dendritic lithium growth, a hallmark of localized current distribution irregularities and interfacial instability. Such dendritic structures not only pose a risk of piercing the separator membrane, but their persistent fracturing and regrowth processes continuously consume active lithium and electrolyte, leading to rapid capacity decay and diminished coulombic efficiency. (**Fig. S14, S15**).

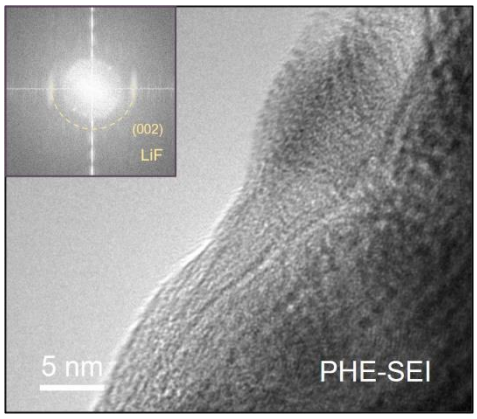

Figure S16. Cryo-TEM image of SEI formed by PHE electrolyte.

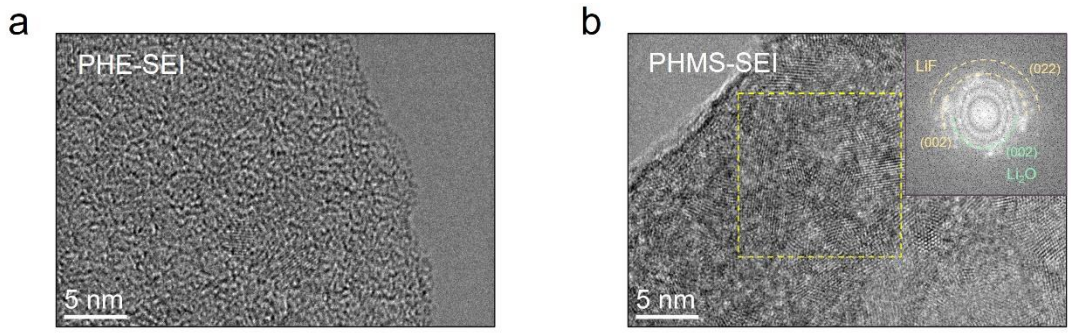

Figure S17. HRTEM images of SEI formed by (a) PHE and (b) PHMS electrolytes.

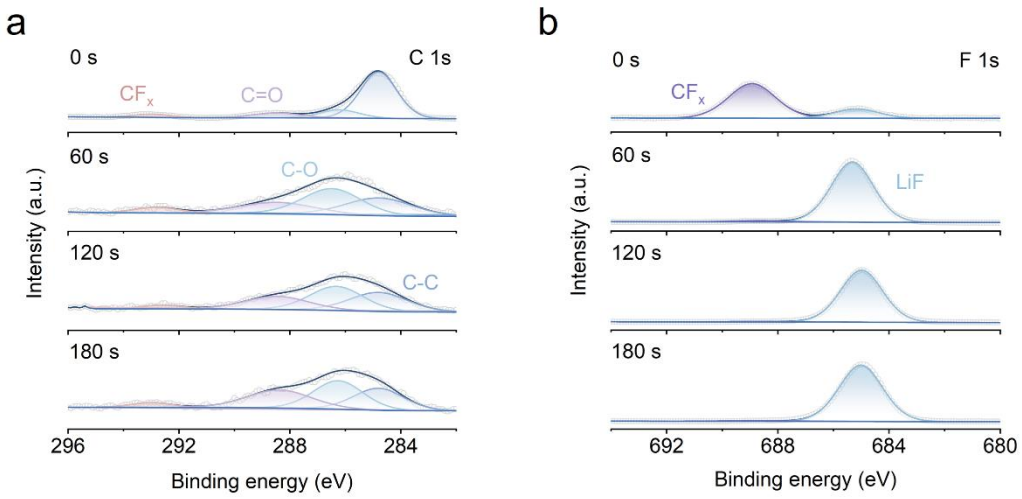

Figure S18. (a) C 1s, (b) F 1s spectra of lithium anode after cycling in PHE electrolyte.

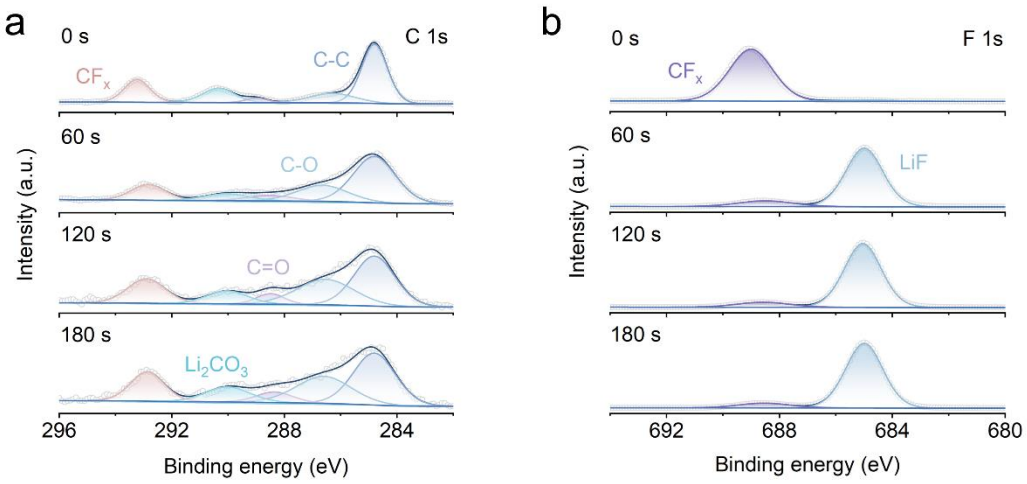

Figure S19. (a) C 1s, (b) F 1s spectra of lithium anode after cycling in $PHMoS_2$ electrolyte.

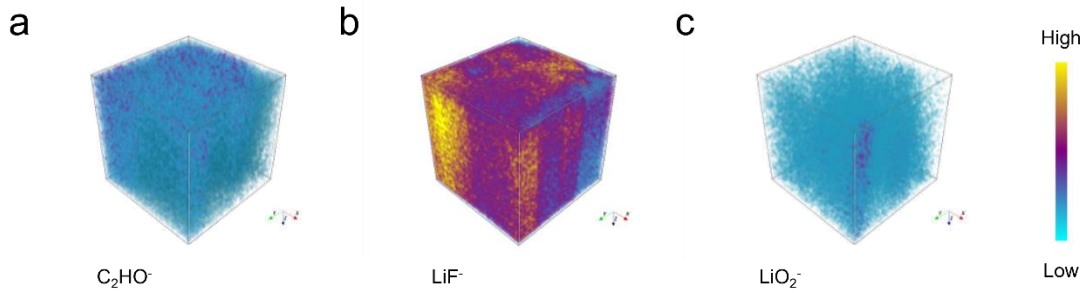

Figure S20. (a)-(c) ToF-SIMS analyses of lithium anode after cycling in PHE electrolyte.

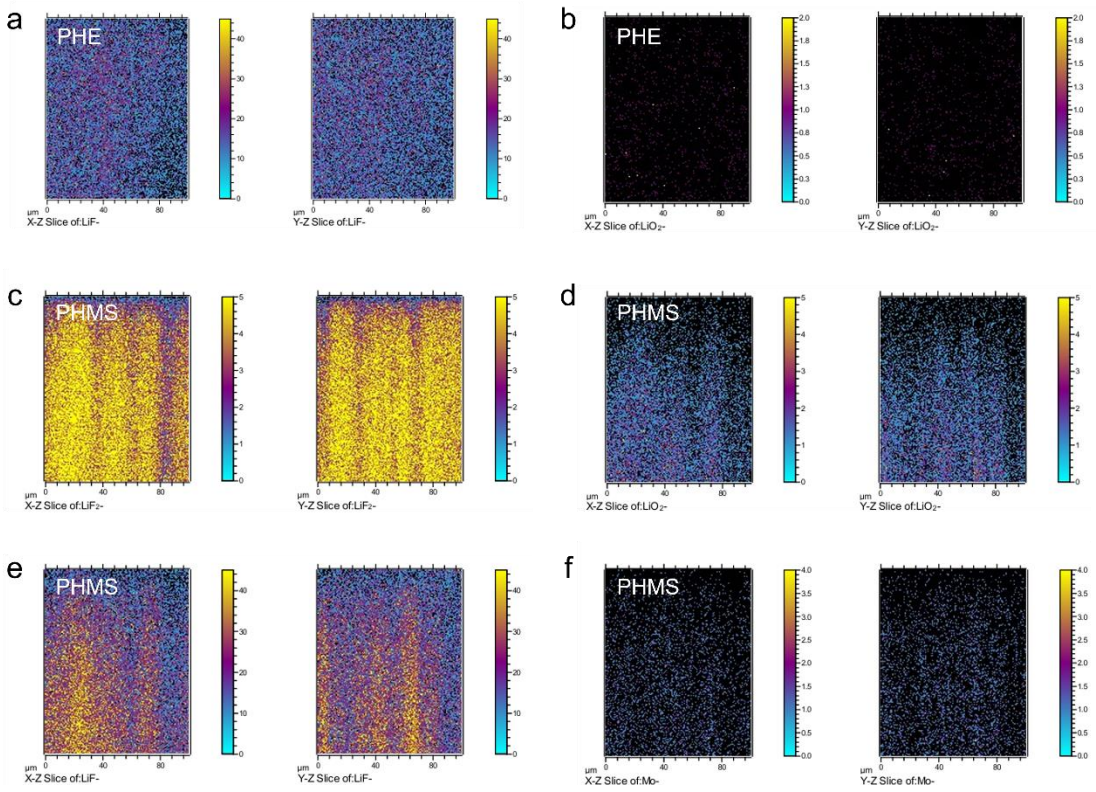

Figure S21. (a)-(b) 2D ToF-SIMS analyses of lithium anode after cycling in PHE electrolyte. (c)-(f) 2D ToF-SIMS analyses of lithium anode after cycling in PHMS electrolyte.

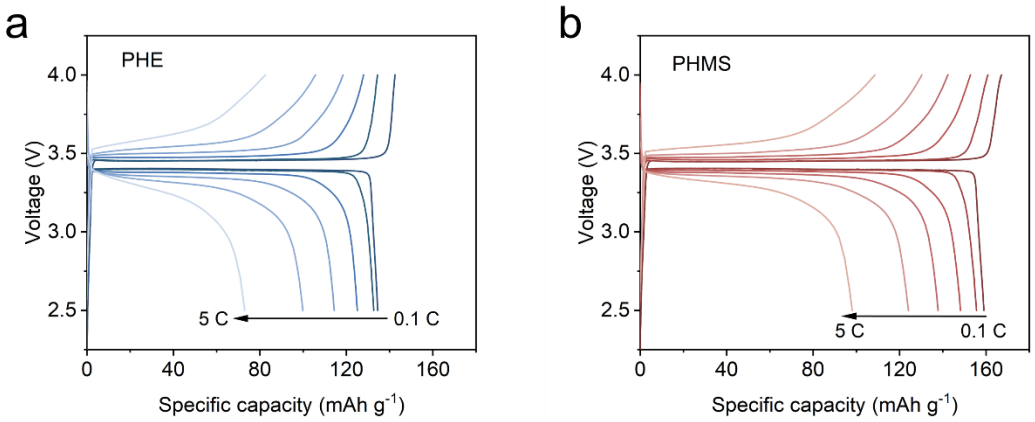

Figure S22. (a) Charge-discharge profiles of the LFP|PHE|Li cell at different rates. (b) Charge-discharge profiles of the LFP|PHMS|Li cell at different rates.

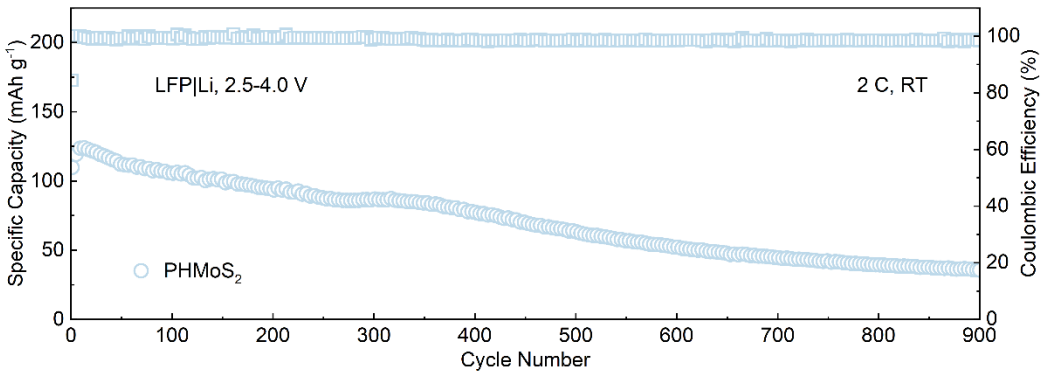

Figure S23. Cycling performance of LFP|PHMoS$_2$|Li cell at 2 C.

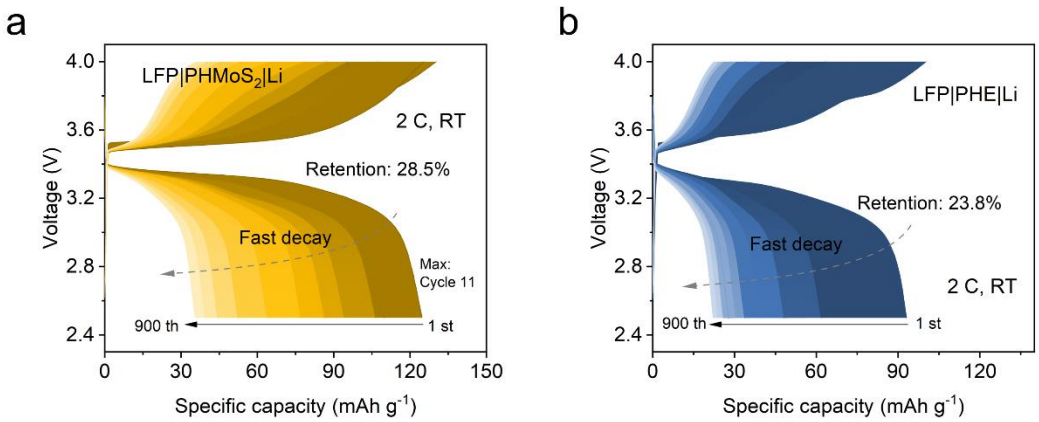

Figure S24. Charge-discharge profiles of the (a) LFP|PHMoS$_2$|Li and (b) LFP|PHE|Li cells at 2 C.

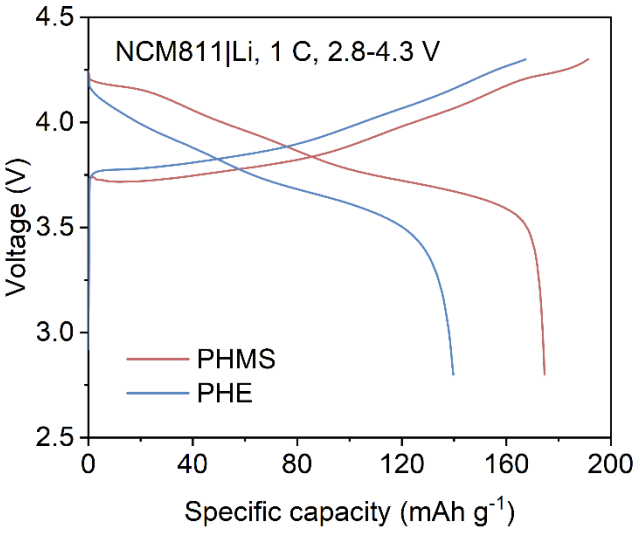

Figure S25. Charge-discharge profiles of the NCM811||Li cells at 1 C.

Figure S26. The image of LFP|PHMS|Li pouch cell.